Optimum Design Guidelines on MPD Thrusters Around Critical Current

IEPC-2011- 033

Presented at the 32nd International Electric Propulsion Conference,
Wiesbaden • Germany
September 11 – 15, 2011

Yoshitaka Takahashi[*], Ryo Ohtake[†], Masakatsu Nakane[‡] and Yoshio Ishikawa[§]
Nihon University, Fumabashi, Chiba 274-8501, Japan

Kenichi Kubota[¶]
Japan Aerospace Exploration Agency, Chofu, Tokyo 182-8522, Japan

and

Ikkoh Funaki[#]
Japan Aerospace Exploration Agency, Sagamihara, Kanagawa 229-8510, Japan

Abstract: We conducted optimizations along with numerical simulations with the objective of identifying MPD discharge chamber configurations that maximize thrust efficiency. Two mechanisms are used for accelerating the plasma in a MPD thruster: aerodynamic acceleration and electromagnetic acceleration. When the discharge current is lower than the critical current, aerodynamic acceleration is dominant; when it is higher than the critical current, electromagnetic acceleration is dominant. Thus, the acceleration mode varies with the discharge current intensity, indicating that the criteria for the design of the discharge chamber configuration vary with the current intensity. The discharge chamber configuration was therefore optimized in the following procedure to observe the changes in the optimized discharge chamber configuration before and after the transition of the acceleration mode. The discharge chamber configuration was limited to a straight-flare shape, and the internal flow was assumed to be two-dimensional axially symmetric. The design variables were certain discharge chamber configuration parameters and the discharge current value, and the objective function was thrust efficiency. The discharge current was varied in the range 4000 to 8000 A to include the critical current value. Differential Evolution was employed as the optimization procedure, and the response surface method was employed to reduce the number of CFD calculations. Three optimized configurations were obtained as a result of this optimization before and after the transition of the acceleration mode. These were (1) the configuration for operation before the transition, in which the main acceleration mode was aerodynamic, (2) the configuration for the operation after transition, in which electromagnetic acceleration was dominant, and (3) the configuration for operation when both aerodynamic and electromagnetic acceleration modes are employed.

[*] Graduate Student, Department of Aerospace Engineering, takahashi@stone.aero.cst.nihon-u.ac.jp
[†] Graduate Student, Department of Aerospace Engineering, takahashi@stone.aero.cst.nihon-u.ac.jp
[‡] Assistant Professor , Department of Aerospace Engineering, m_nak@stone.aero.cst.nihon-u.ac.jp
[§] Professor, Department of Aerospace Engineering, yishi@stone.aero.cst.nihon-u.ac.jp
[¶] Researcher, Aerospace Research and Development Directorate, kkubota@chofu.jaxa.jp
[#] Associate Professor, Institute of Space and Astronautical Science, funaki@isas.jaxa.jp

Nomenclature

$\mathbf{B}$	=	magnetic flux density
ρ	=	mass density
$\mathbf{u}$	=	velocity
p	=	pressure
$\mathbf{I}$	=	unit tensor
$\mathbf{j}$	=	current density
$\overline{\tau}$	=	viscous stress tensor
$\mathbf{E}$	=	electric field
λ	=	thermal conductivity
T	=	temperature
γ	=	specific heat ratio
R	=	gas constant
μ_0	=	magnetic permeability
σ	=	electric conductivity
ε	=	energy density
V	=	discharge voltage
F_{all}	=	thrust
η	=	thrust efficiency
P	=	input power
J	=	discharge current
$d\mathbf{S}$	=	surface element
$d\mathbf{l}$	=	line element
r_{in}	=	inlet anode radius
r_{out}	=	outlet anode radius
r_{c}	=	cathode radius
L_{st}	=	anode straight section length
L_{c}	=	cathode length
L_{a}	=	overall length of discharge chamber
θ	=	diverging angle
J_{c}	=	critical current
F_{magneto}	=	electromagnetic force
F_{aero}	=	aerodynamic force

I. Introduction

MAGNETOPLASMADYNAMIC (MPD) thrusters are one type of electric thruster. This class of thrusters offers the highest thrust density and specific impulse and is expected to shorten the length of interplanetary missions. A viable version of these thrusters has yet to be developed, however. One reason is their low thrust efficiency.

The electrodes of the discharge chamber of a self-induced magnetic field type MPD thruster, which is the focus of the present study, have a coaxial structure consisting of a rod-shaped cathode along the axis, surrounded by an anode. The current paths, the magnetic field distribution, and the discharge voltage in the thruster all vary with the discharge chamber configuration (electrode shape). One can then expect that optimizing the discharge chamber configuration will improve the thrust efficiency. We have been employing an optimization procedure based on numerical simulations in search of the discharge chamber configuration yielding the greatest thrust efficiency.[1-3]

Two mechanisms of plasma acceleration are used in a MPD thruster: the aerodynamic acceleration mode and the electromagnetic acceleration mode. Below a certain critical discharge current level, the aerodynamic acceleration dominates, but when the discharge current is high, the electromagnetic acceleration dominates.[4] The fact that these two modes exist implies that they require different criteria in the design of the discharge chamber configuration.

We carried out optimizations of the discharge chamber configuration, as described below, to observe changes in the optimized discharge chamber configuration before and after the transition of acceleration modes. The design variables were the discharge chamber configuration and the discharge current, and the objective function was the thrust efficiency. The discharge chamber configuration variables were defined to describe a straight-flare shape. The discharge current range was set to include the critical current value. Differential Evolution (DE), a technique based

on the Genetic Algorithm (GA), was employed as the optimization procedure, and the response surface method was applied to reduce the number of CFD calculations.

II. Acceleration Modes and the Critical Current

The Lorentz force generated by the interaction between the discharge current and the resulting self-induced magnetic field in self field MPD thrusters accelerates the propellant. The Lorentz force is low under low discharge current because the induced magnetic field is weak. This is why the aerodynamic forces are the dominant acceleration mechanism in a low-electric-powered MPD thruster. As the discharge current increases, the acceleration mechanism transitions to be electromagnetic. This transition manifests as a change in the voltage–current characteristic. That is, the discharge voltage increases with the discharge current, but is known to show an abrupt acceleration beyond a certain level of the discharge current. This threshold is called the critical current J_c and can be found by using the change in the slope of the increasing discharge volatage.[5]

III. Modeling

A. Assumptions of the flowfield

The following assumptions are made for the calculations in a computational fluid dynamics (CFD) analysis of the plasma flow in a MPD thruster:

· The flowfield is a two-dimensional axially symmetric flow of a single-fluid model.
· The model takes into account the thermal conductivity and viscosity of the fluid.
· The sheath voltage is constant at 20 V.
· Multi-step ionization and the Hall effect are neglected.
· The wall is thermally insulated.
· The plasma is completely ionized.
· Single temperature model is assumed.
· Local thermal equilibrium is preserved.

B. Governing equations

The governing equations for the interior of the MPD thruster are derived from the magnetohydrodynamic equations as shown below.

Mass conservation equation:

$$\frac{\partial \rho}{\partial t} + \nabla \cdot (\rho \mathbf{u}) = 0 \,. \tag{1}$$

Momentum conservation equation:

$$\frac{\partial \rho \mathbf{u}}{\partial t} + \nabla \cdot (\rho \mathbf{u}\mathbf{u} + p\mathbf{I}) = \mathbf{j} \times \mathbf{B} + \nabla \cdot \bar{\tau} \,. \tag{2}$$

Total energy conservation equation:

$$\frac{\partial \varepsilon}{\partial t} + \nabla \cdot \left[(\varepsilon + p)\mathbf{u} \right] = \mathbf{j} \cdot \mathbf{E} + \nabla \cdot (\bar{\tau}) + \nabla \cdot (\lambda \nabla T) \,, \tag{3}$$

where

$$\varepsilon = \frac{1}{2}\rho \mathbf{u}^2 + \frac{p}{\gamma - 1} \,. \tag{4}$$

Equation of state (fully-ionization):

$$p = 2\rho RT \,. \tag{5}$$

Maxwell's equation:

$$\nabla \times \mathbf{B} = \mu_0 \mathbf{j} \,. \tag{6}$$

Ohm's law:

$$\mathbf{j} = \sigma (\mathbf{E} + \mathbf{u} \times \mathbf{B}) \,. \tag{7}$$

Induction equation

$$\frac{\partial \mathbf{B}}{\partial t} = \nabla \times (\mathbf{u} \times \mathbf{B}) - \nabla \times \left(\frac{1}{\sigma \mu_0} \nabla \times \mathbf{B} \right). \tag{8}$$

C. Calculation conditions

The calculation conditions were set as follows on the basis of actual operating conditions.

Table 1. Calculation conditions

Propellant	Argon
Mass flow rate $\dot{m}$ [g/s]	0.8
Discharge current J [A]	$4000 \le J \le 8000$
Sheath voltage V_s [V]	20
Inlet temperature T_{in} [K]	10000

IV. Formulation of the Optimization Problem

A. Evaluation function

The purpose of this study was to improve the thrust efficiency. Therefore, thrust efficiency η was used as the evaluation function to be maximized. Thrust efficiency η is defined as follows:

$$\text{maximize :} \quad \eta = \frac{{F_{all}}^2}{2\dot{m}P} = \frac{{F_{all}}^2}{2\dot{m}JV}, \tag{9}$$

where thrust F_{all} and the discharge voltage V are physical quantities only available for evaluating after the CFD analysis. Thrust F_{all} was estimated using the area integral of the momentum component in the axial direction and pressure at the discharge chamber outlet. Discharge voltage V was estimated with line integrations from the negative electrode to the positive electrode by the following formulas:

$$F_{all} = \int_{outlet} (\rho \mathbf{u}\mathbf{u} + p\mathbf{I}) \cdot d\mathbf{S} \tag{10}$$

$$V = \int_{cathode}^{anode} \mathbf{E} \cdot d\mathbf{l} + V_s \tag{11}$$

B. Design variables

This study carried out an optimization to maximize the thrust efficiency. The design variables were discharge chamber configuration parameters and the discharge current value. The chamber was limited to the straight-flare shape used in experiments. The four selected discharge chamber configuration parameters were those shown in Fig. 1, as suggested in the previous literature[1]: inlet radius r_{in}, outlet radius r_{out}, straight section length L_{st}, and cathode length L_c. Together with the variable of the discharge current value, there were a total of five design variables. Table 2 shows the ranges of the design variables. Once the operating conditions and the discharge chamber configuration were designated, we could estimate an approximate value for the critical current, which was estimated at approximately 5000 to 6000 A in the various operating conditions and discharge chamber configurations tested in this study. Therefore, the designated range for the discharge current was set to 4000 to 8000 A so as to include the acceleration mode transition region.

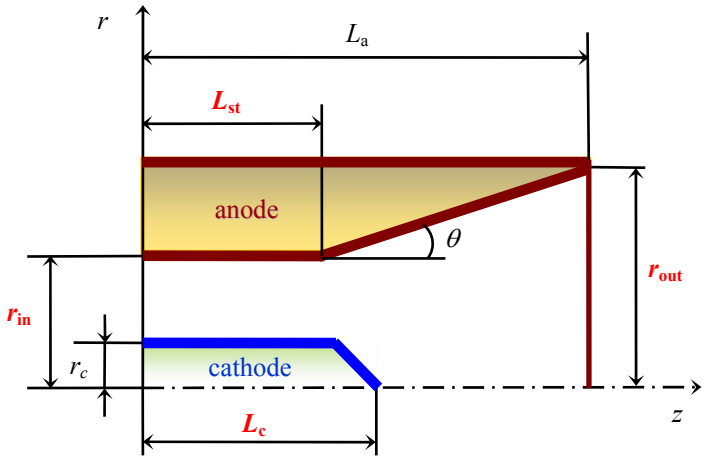

Figure 1. Discharge chamber configuration parameters

Table 2. Ranges of the design variables

Inlet radius r_{in} [cm]	$1.0 \le r_{in} \le 2.0$
Outlet radius r_{out} [cm]	$2.0 \le r_{out} \le 3.5$
Straight section length L_{st} [cm]	$1.0 \le L_{st} \le 4.0$
Cathode length L_c [cm]	$1.0 \le L_c \le 4.8$
Discharge current J [A]	$4000 \le J \le 8000$

The cathode radius r_c was assumed to be constant at 0.4 cm and the total anode length L_a was assumed to be constant at 6.0 cm. Another imposed constraint on the design variables was that the diverging angle of the anode was $\theta \ge 5$ deg.

V. Optimization Method

A. Optimization with the Response Surface Method

The response surface method was used in this study as the optimization procedure.[6, 7] This procedure expresses the relation between the design variables and their evaluation values at some appropriate number of sample points with an approximation surface. Here, the approximation surface expressed the relations of the discharge chamber configuration and the discharge current value to the thrust efficiency. One could reduce the number of CFD calculations by finding the maximum point on this approximation surface. This allowed us to greatly reduce the time needed for the optimization.

The kriging model, a type of response surface method, was employed in this study.[8] A kriging model creates an approximation surface that passes through all of the sample points and allows interpolation between them. A value can be predicted for any desired location. Therefore, it is well suited to computational experiments, where there are no measurement errors.

To create as accurate an approximation surface as possible, it is best to begin by indexing the entire region and then distributing sample points to capture the characteristics of the solution space. Latin hypercube sampling, an experimental design method, was employed in this study to select the sample locations.[9]

B. Global optimization

A kriging model creates an interpolation approximation equation that provides values matching all of the sample points. However, the solution space obtained in the approximation equation may have multiple peaks complex. A global optimization must be performed to search out the maximum value points in the created approximation surface.

Thus, Differential Evolution (DE), a Genetic Algorism procedure, was used here to carry out the global optimization.[10]

C. Constraint of input power

It is well known that the thrust efficiency of MPD thrusters rises with the increase in the input electric power input. Therefore, if we perform an ordinary optimization, the optimal solution is one with maximized input electric power. For this reason, in this study, the input electric power was divided into several regions and an optimization was performed within each range of input electric power. The constraint expressed in the following equation was imposed on the input electric power P. Convenient values were selected for the power magnitudes P^* and ΔP and the optimizations were performed within the given range.

$$P^* \le P \le P^* + \Delta P \tag{12}$$

The calculation in this study was performed using ΔP = 10 kW.

VI. Example of an Optimization Calculation

Figure 2 shows the thrust efficiencies for the individuals (discharge chamber configurations) obtained by 271 CFD calculations in this optimization process. The horizontal axis is the input electric power. The red points in the graph are the discharge chamber configurations that showed the highest thrust efficiencies at each input electric power: that is, these were the optimal configurations at each respective input electric power. In the region below the input electric power of 118 kW, the discharge current was constant at 4000 A for all the optimal configurations. Similarly, above the input electric power of 278 kW, the discharge current was constant at 8000 A for many of the optimal configurations. Since this study addressed the transition region between acceleration modes, it would be off-topic to discuss the regions below 118 kW or above 278 kW, which are far from the critical current level of 5000 to 6000 A (input electric power 155–184 kW).

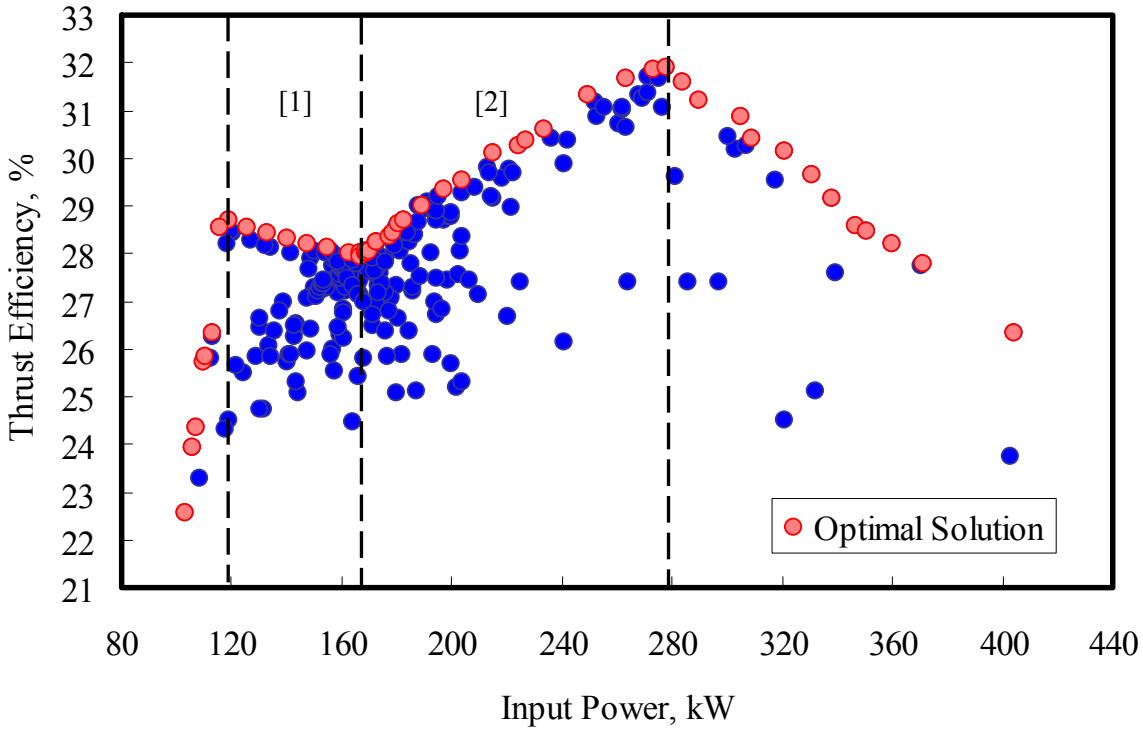

Figure 2. Thrust efficiencies at various input electric power levels

A. Changes in discharge chamber configuration and discharge current

Figure 2 can be divided into Region [1] (118–167 kW) and Region [2] (167–278 kW). A single configuration was indicated to be optimal in Region [1] (118–167 kW), and two configurations were indicated as optimal in Region [2], in the ranges 167 to 278 kW and 167 to 177 kW.

Figure 3 shows the optimal configuration for Region [1] (118–167 kW). The inlet radius r_{in} was 1.15 cm, close to the lower limit, the outlet radius r_{out} was 2.39 cm, and the straight section length L_{st} and cathode length L_c were at the lower limit, 1.00 cm. The discharge chamber configuration did not vary with the increase in input electric power; the only variation was the discharge current, which increased from 4000 A to 5300 A. This is referred to as the "short cathode type" hereinafter.

Two configurations were obtained for Region [2] (168–278 kW). Neither showed much variation in configuration with the increase in input electric power; as in Region [1], only the discharge current varied.

Figure 4 shows the configuration that provided the maximum thrust efficiency throughout Region [2] (168–278 kW). The configuration is as follows: the inlet radius r_{in} was near the upper limit, 2.00 cm, the outlet radius r_{out} was near the upper limit, 3.50 cm, and the straight section length L_{st} was near the lower limit. The cathode length L_c was long, at 3.43 to 4.24 cm. This configuration is called the "long cathode type" hereinafter and was generated in the 5700–8000 A range of the discharge current.

Figure 5 shows the optimal configuration for the maximum thrust efficiency in the lower portion of Region [2], 167 to 177 kW. The optimal configuration here is as follows: the inlet radius r_{in} was the upper limit, the outlet radius r_{out} was 2.62 to 2.80 cm, and the straight section length L_{st} was the lower limit. The cathode length L_c was an intermediate value at 2.0 cm, the "semi-short cathode type" hereinafter. The semi-short cathode type was generated in the 5400 to 5600 A range of the discharge current.

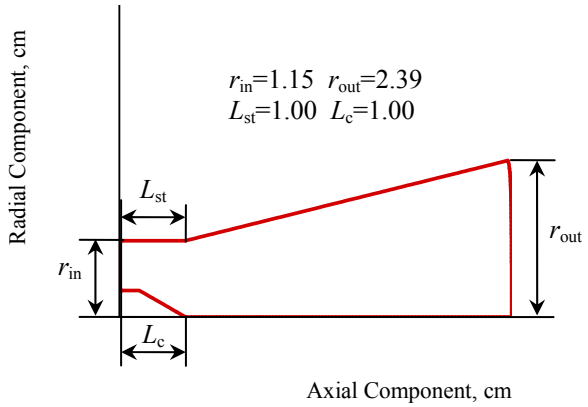

Figure 3. Optimal configuration for Region [1] (short cathode type)

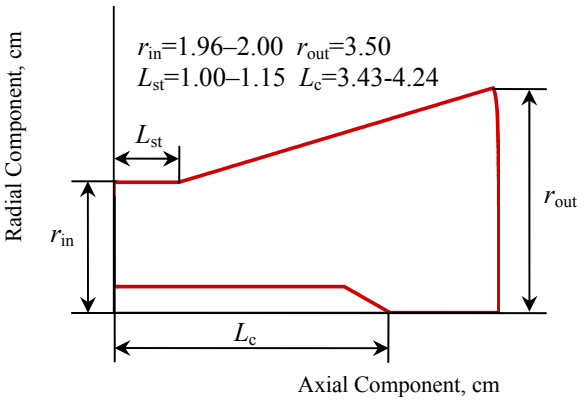

Figure 4. Optimal configuration 1 for Region [2] (long cathode type)

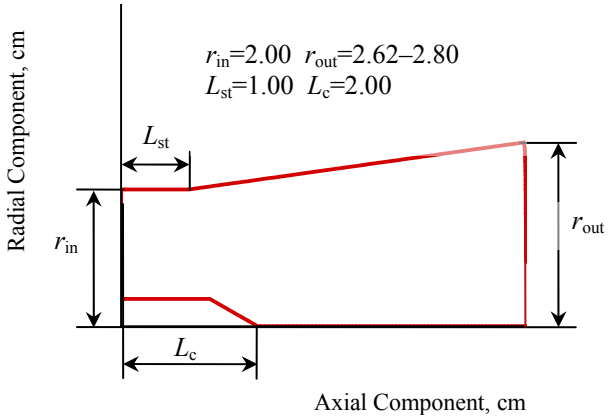

Figure 5. Optimal configuration 2 for Region [2] (semi-short cathode type)

B. Classification of optimal configurations by the critical current

Let us begin with some observations about the acceleration modes of the three optimal configurations. Figures 6 to 8 show the voltage–current characteristics for these configurations. The critical current at the optimal configurations was obtained from these figures at two levels, near 5200 A for the short cathode type and near 5600 A for the long cathode and semi-short cathode types.

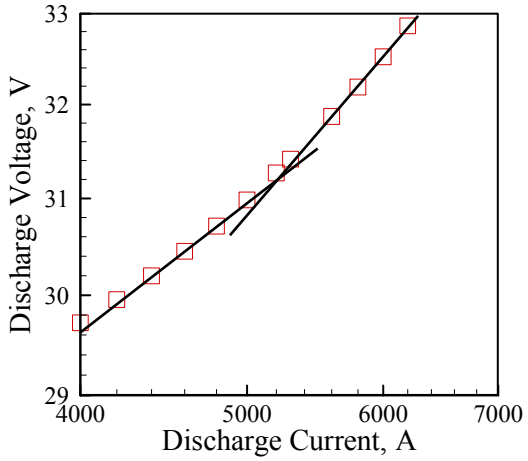

Figure 6. Voltage–current characteristic for short cathode type (J_c=5200 A)

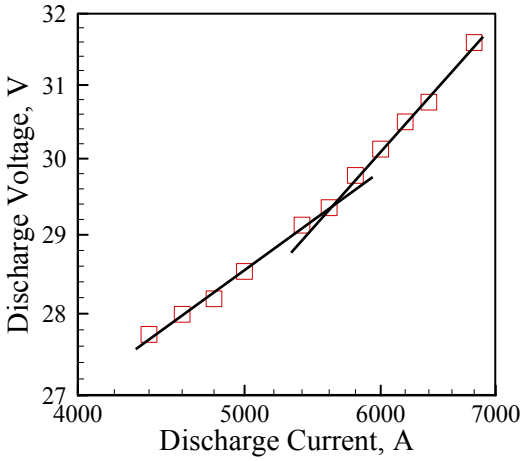

Figure 7. Voltage-current characteristic for long cathode type (J_c=5600 A)

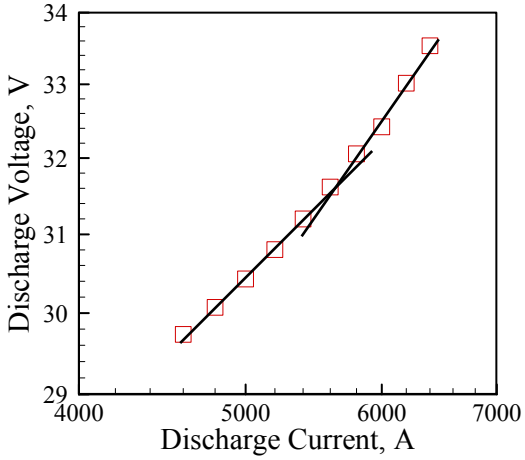

Figure 8. Voltage–current characteristic for semi-short cathode type (J_c=5600 A)

To observe the acceleration mode under each of the optimal discharge chamber configurations, Fig. 9 was drawn to show the summary of the electromagnetic thrust and the aerodynamic thrust under each configuration. The horizontal axis is the discharge current, not the input electric power. The electromagnetic thrust F_{magneto} and the aerodynamic thrust F_{aero} are defined by the following expressions:

$$F_{magneto} = \int_V \left(\mathbf{j}\times\mathbf{B}\right)_z \cdot dV \tag{13}$$

$$\begin{aligned} F_{aero} &= \int_{outlet} \left(\rho\mathbf{uu} + p\mathbf{I}\right)\cdot d\mathbf{S} - \int_V \left(\mathbf{j}\times\mathbf{B}\right)_z \cdot dV \\ &= F_{all} - F_{magneto} \end{aligned} \tag{14}$$

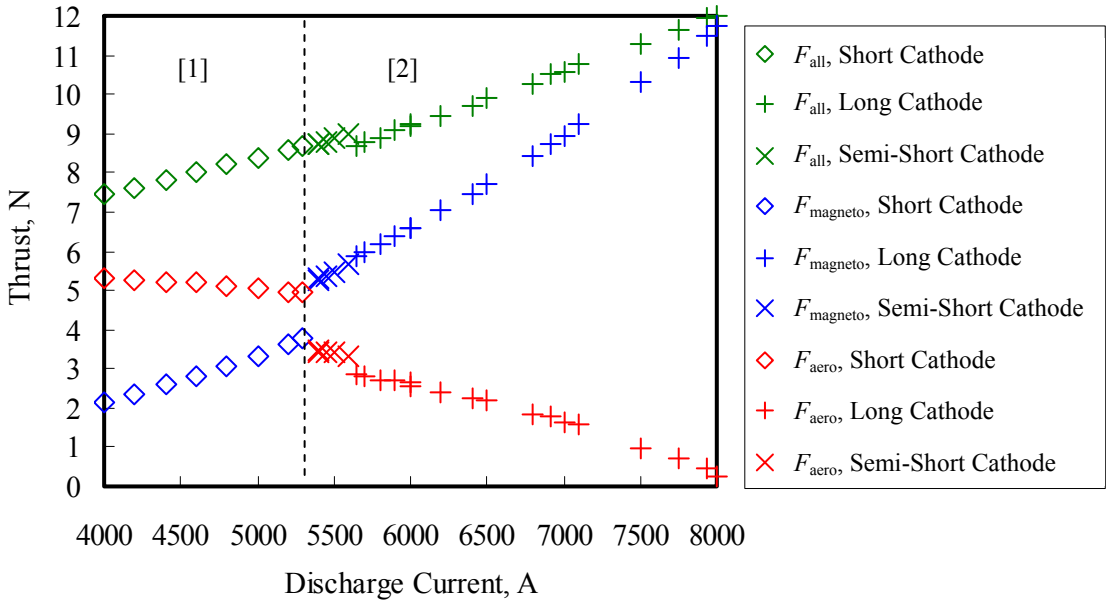

Figure 9. Summary of the thrust–current relationship

Figure 9 shows a reversal in the relative magnitudes of $F_{magneto}$ and F_{aero} in the vicinity of 5300 A. In other words, this is the borderline between the two acceleration modes.

In Region [1] (4000–5300 A), where the short cathode type was optimal, the critical current was below 5200 A, and F_{aero} exceeded $F_{magneto}$. Figures 10 and 11 show the current paths and flow speed distribution, respectively, in the short cathode type at 4000 A. The current paths reveal that the current was concentrated in the vicinity of the inlet. In other words, the current paths had the same distribution as that of an electrothermal thruster. This implies that reducing the inlet radius and the cathode length would likely improve the efficiency of the aerodynamic acceleration mode in the short cathode type.

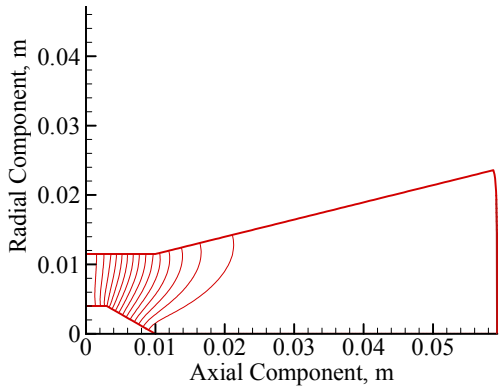

Figure 10. Current paths for short cathode type (4000 A)

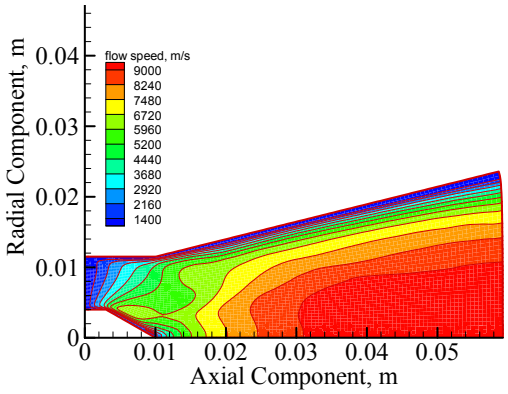

Figure 11. Flow speed distribution for short cathode type (4000 A)

However, the long cathode type for critical currents above 5600 A was the optimal one for currents above 5700 A, and $F_{magneto}$ becomes higher than F_{aero}. The characteristics of the long cathode type exactly match the optimal configuration in the region we previously reported, where the electromagnetic acceleration was dominant.[1] As in the previous report, the inlet radius and outlet radius were the maximum size and the cathode length was large. Figures 12 and 13 show the current paths and flow speed distribution, respectively, in the long cathode configuration. The previous research indicated that the optimal configuration when electromagnetic acceleration dominates has a long cathode and a large gap between the cathode and the anode. We also know that this configuration moderates the

concentration of current in the discharge chamber, as shown in Fig. 12. This can explain why the main acceleration mode in the long cathode type is electromagnetic acceleration, which makes it the optimal configuration for the region above the critical current.

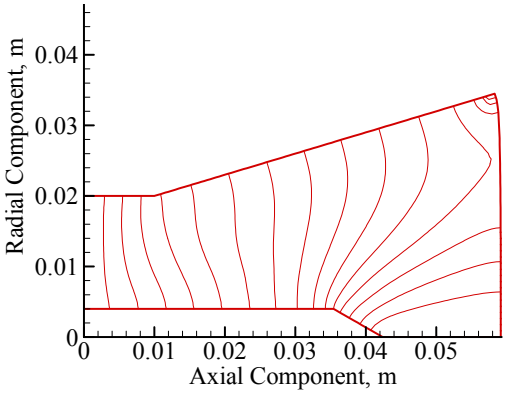

Figure 12. Current paths for long cathode type (8000 A)

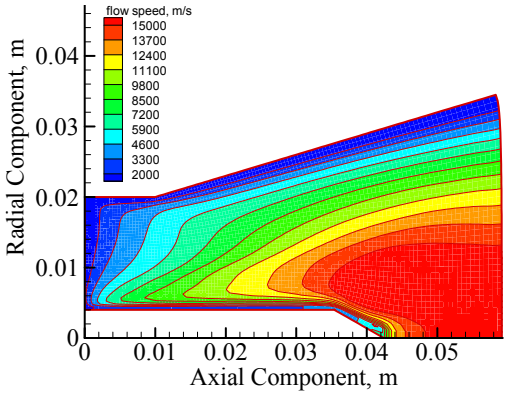

Figure 13. Flow speed distribution for short cathode type (8000 A)

Let us conclude with a few observations regarding the semi-short cathode type, below the critical current, 5600 A, which is the optimal configuration for currents in the 5400 to 5600 A range. In this configuration, F_{magneto} exceeds F_{aero}; but as the share of F_{magneto} was only 60 to 63% of the entire thrust, it would be an exaggeration to call F_{magneto} dominant. Figures 14 and 15 show the current paths and flow speed distribution, respectively, for the semi-short cathode type. As these figures show, the results are intermediate between the short cathode type and the long cathode type. Also, according to Fig. 9, F_{aero} accounts for a larger share of the force than in the long cathode type. In the case of the semi-short cathode type, the majority of acceleration is provided by the aerodynamic component, but the electromagnetic component cannot be neglected, and so this configuration is deemed intermediate.

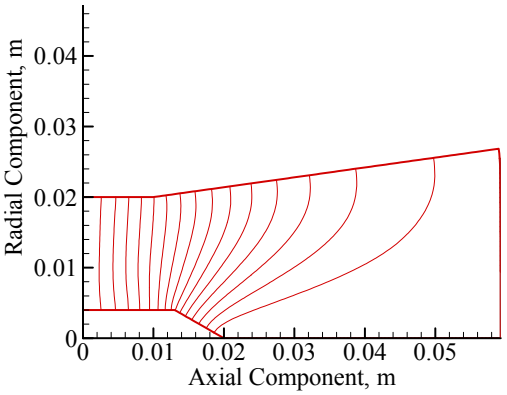

Figure 14. Current paths for semi-short cathode type (5400 A)

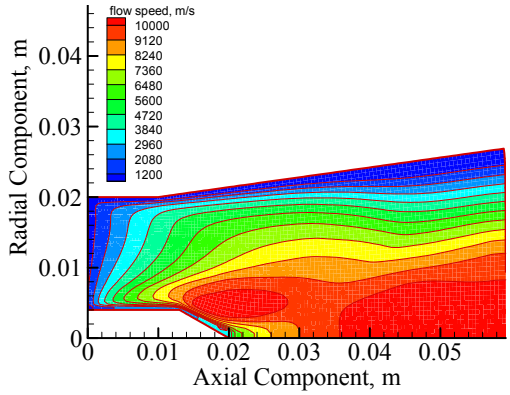

Figure 15. Flow speed distribution for semi-short cathode type (5400 A)

VII. Conclusion

This study employed a two-dimensional axially symmetric model of a flowfield in a MPD thruster using a discharge chamber configuration and discharge current (4000–8000 A) as design variables to conduct an optimization to achieve maximum thrust efficiency.

This optimization showed that the transition from the aerodynamic acceleration mode to the electromagnetic acceleration mode occurred around a discharge current of 5300 A. A short cathode type in the discharge chamber was the optimal configuration before the transition of the acceleration mode. Two optimal configurations were

obtained post-transition: a long cathode type and a semi-short cathode type. The relations between these configurations and the critical current were also examined.

The Hall effect, which was neglected in this flowfield model, exercises a significant influence above the critical current. In the future, therefore, models must be optimized while taking into account this effect.

References

[1] Nagao, M., Kubota, K., Nakane, M., Ishikawa, Y. and Funaki, I., "Boostuing MPD Thruster Propulsion Efficiency through Optimization," IEPC paper 2009-229, 2009.

[2] Nakane, M., Hayashi, T., Ishilawa, Y., Funaki, I. and Toki, K., "Extraction of Magnetoplasmadynamic Thruster Design Guidelines through Optimization", Trans. JSASS Space Tech. Japan, Vol. 7, 2009, pp.Pb_11-Pb_16.

[3] Nakane, M., Nagao, M., Ishikawa, Y., Kubota, K. and Funaki, I., "Nozzle Shape Optimization for an MPD Thruster Using a Two-Dimensional Axisymmetric Flow Modle," Journal of the Japan Society for Aeronautical and Space Sciences, Volume 59, Issue 687, pp. 90-96, 2011. (In Japanese)

[4] Kuriki, K. and Arakawa, Y., "*Introduction to Electric Propulsion*," University of Tokyo Press, Tokyo, 2003, pp.124-129. (In Japanese)

[5] Kubota, K., Funaki I., and Okuno, Y., "Numerical Study on the Transition between Electrothermal and Electromagnetic Acceleration Modes in an MPD Thruster," Journal of the Japan Society for Aeronautical and Space Sciences, Vol.54, No.635, pp.535-541, 2006. (In Japanese)

[6] Chiba, K., Imamura, T., Amemiya, K. and Yamamoto, K., "Design Optimization of Shielding Effect for Aircraft Engine Noise," Journal of Environment and Engineering," **2**, pp.567-577, 2007.

[7] Jeong, S., Murayama, M. and Yamamoto, K, "Efficient Optimization Design Method Using Kriging Model, Journal of Aircraft," **42**, pp 413-420, 2005.

[8] Timothy, W. S., Timothy, M. M., John, J. K. and Farrokh M., "Kriging models for Global Approximation in Simulation-Based Multidisciplinary Design Optimization", AIAA J., **39**-12, pp. 2233-2241, 2001.

[9] Art, B. O., "Orthogonal Arrays for Computer Experiments, Integration and Visualization, Statistica Sinica," **2**, pp.439-452, 1992.

[10] Ito, M. and Tanaka, M., "A comparative study of particle swarm optimization, differential evolution, real-coded genetic algorism on function optimization," Mem.Konan Univ., Sci. and Eng.ser., Vol.52(1), pp.125-135, 2005. (In Japanese)